

Quasi-two-dimensional isotropic laser cooling of atoms for quantum sensing

Xiao Zhang(张孝), Yi Song(宋屹), Yuan Sun(孙远), and Liang Liu(刘亮)

Citation: Chin. Phys. B, 2025, 34 (**8**): 084202. DOI: 10.1088/1674-1056/add4f7
http://cpb.iphy.ac.cn; http://iopscience.iop.org/cpb

What follows is a list of articles you may be interested in

Phase-modulated dynamical decoupling sequences robust to systematic amplitude error

Sijie Chen(陈思婕), Guanxing Chen(陈官幸), Jiahao Huang(黄嘉豪), Peiliang Liu(刘培亮), Min Zhuang(庄敏), and Chaohong Lee(李朝红)
Chin. Phys. B, 2025, 34 (**7**): 074202. DOI: 10.1088/1674-1056/adcd43

Design of a high sensitivity and wide range angular rate sensor based on exceptional surface

Xinsheng Ding(丁鑫圣), Wenyao Liu(刘文耀), Shixian Wang(王师贤), Yu Tao(陶煜), Yanru Zhou(周彦汝), Yu Bai(白禹), Lai Liu(刘来), Enbo Xing(邢恩博), Jun Tang(唐军), and Jun Liu(刘俊)
Chin. Phys. B, 2024, 33 (**8**): 084204. DOI: 10.1088/1674-1056/ad4324

A novel dual-channel thermo-optic locking method for the whispering gallery mode microresonator

Wenjie Fan(范文杰), Wenyao Liu(刘文耀), Ziwen Pan(潘梓文), Rong Wang(王蓉), Lai Liu(刘来), Enbo Xing(邢恩博), Yanru Zhou(周彦汝), Jun Tang(唐军), and Jun Liu(刘俊)
Chin. Phys. B, 2024, 33 (**5**): 054206. DOI: 10.1088/1674-1056/ad225f

Enhanced phase sensitive amplification towards improving noise immunity

Hui Guo(郭辉), Zhi Li(李治), Hengxin Sun(孙恒信), Kui Liu(刘奎), and Jiangrui Gao(郜江瑞)
Chin. Phys. B, 2023, 32 (**5**): 054204. DOI: 10.1088/1674-1056/acbdeb

Tunable phonon-atom interaction in a hybrid optomechanical system

Yao Li(李耀), Chuang Li(李闯), Jiandong Zhang(张建东), Ying Dong(董莹), and Huizhu Hu(胡慧珠)
Chin. Phys. B, 2023, 32 (**4**): 044213. DOI: 10.1088/1674-1056/acb9ea

---

Quasi-two-dimensional isotropic laser cooling of atoms for quantum sensing

Xiao Zhang(张孝)[1,2,†,‡], Yi Song(宋屹)[1,2,†], Yuan Sun(孙远)[1,2], and Liang Liu(刘亮)[1,2,§]

[1] *CAS Key Laboratory of Quantum Optics and Aerospace Laser Technology and Systems Department, Shanghai Institute of Optics and Fine Mechanics, Chinese Academy of Sciences (CAS), Shanghai* 201800, *China*
[2] *University of Chinese Academy of Sciences, Beijing* 100049, *China*

(Received 19 February 2025; revised manuscript received 30 April 2025; accepted manuscript online 7 May 2025)

Isotropic laser cooling (ILC) is widely recognized for its distinct advantages and demonstrates significant potential in quantum precision measurements and quantum sensing technologies. The morphology and density distribution of the cold atomic cloud generated by ILC are strongly influenced by the distribution of cooling light and the structural geometry of the cavity, making precise characterization and optimization of cold atom distribution essential for practical applications. In this paper, we present an innovative flat diffuse cavity design with the dimensions approximating a quasi-two-dimensional configuration, which generates a sheet-like isotropic laser field inside the cavity through diffuse reflections. We thoroughly characterized the system's performance under different optical parameter settings. A two-dimensional (2D) movable detection system was employed to detect the quasi-two-dimensional distribution of cold atoms. These results demonstrate the ability of ILC to produce diverse morphological and density distributions of cold atoms, which we anticipate will be suitable for quantum sensing.

Keywords: quasi-two-dimensional, isotropic laser cooling, quantum sensing

PACS: 42.50.–p, 37.10.De, 37.10.Mn, 32.90.+a

DOI: 10.1088/1674-1056/add4f7 **CSTR:** 32038.14.CPB.add4f7

1. Introduction

Laser cooling has been widely used to prepare cold atoms, which have become a key platform for atomic physics research[1,2] and quantum technologies.[3–5] Isotropic laser cooling (ILC) is a reliable method for producing cold atoms that has garnered significant interest due to its compactness, robustness and all-optical-cooling properties,[6–8] establishing it as an ideal platform for microwave atomic clocks,[9–11] quantum sensing,[12,13] and quantum simulation.[14] Unlike optical molasses or magneto-optical traps (MOTs), ILC does not require a magnetic field or precise alignment of cooling lasers; however, it cannot trap atoms, as the morphological and density distributions of the atomic cloud are determined by the cavity geometry and the injection mode of the cooling beam.

The geometry of the cavity varies depending on the application. Both spherical[15] and cylindrical[16] cavities are extensively utilized in cold atomic clocks, particularly as the cylindrical cavity is valuable since it can integrate the characteristics of diffuse and microwave cavities. A long tube design generates a quasi-one-dimensional distribution of cold atoms, creating promising opportunities for developing a cold atom system analogous to optical fibers.[17] The morphology, density distribution and optical parameter settings of the atomic cloud are crucial for all cavity configurations, as they directly influence the application scenarios, as well as the optical depth (OD) and signal-to-noise ratio (SNR) of the cold atoms. Additionally, the distribution of atoms can be effectively controlled within cavities by adjusting the cooling beam injection mode.[18,19]

In this paper, we present a fresh designed cavity for ILC, with inner dimensions of 100 mm × 50 mm × 6 mm. We characterized the key parameters of this novel ILC system, including the detuning frequencies and the powers of the cooling, repumping and probe beams, as well as their effects on cold atom absorption. Using a 2D movable detection system, we mapped the distribution of cold atoms, exhibiting a quasi-two-dimensional (q2D) profile. This q2D structural design implements a robust and straightforward all-optical method for generating a sheet-like cloud of cold atoms. Compared to other geometries, this configuration provides a larger sensing aperture, making it particularly advantageous for quantum sensing applications. Additionally, this approach may facilitate the construction of large-scale cold atomic arrays.[20] We demonstrated that ILC is applicable to cavities of various shapes, and the ILC method offers flexibility and adaptability for different scenarios. It is anticipated that our findings will contribute to the future development of ILC, supporting quantum sensing

[†] These authors contributed equally to this work.
[‡] Corresponding author. E-mail: zhangxiao@siom.ac.cn
[§] Corresponding author. E-mail: liang.liu@siom.ac.cn

© 2025 Chinese Physical Society and IOP Publishing Ltd. All rights, including for text and data mining, AI training, and similar technologies, are reserved.

and precision measurement technologies.

2. Experimental setup

The hyperfine energy levels of ^{87}Rb atoms used in our experiments are shown in Fig. 1(a). The optical system provides three stable laser beams with different frequencies and powers. The cooling beam is red-detuned by approximately 3Γ below the transition from $|5S_{1/2}, F = 2\rangle$ to $|5P_{3/2}, F' = 3\rangle$, where Γ represents the natural linewidth. The repumping beam is tuned close to the resonance of the $|5S_{1/2}, F = 1\rangle \rightarrow |5P_{3/2}, F' = 2\rangle$ transition, while the probe beam is tuned to resonance with the $|5S_{1/2}, F = 2\rangle \rightarrow |5P_{3/2}, F' = 3\rangle$ transition. The optical system generating these three laser beams is constructed from two laser diodes (LD). The frequencies of both LDs are stabilized using saturation absorption spectroscopy, and the linewidth of each is reduced to a few hundred kilohertz.

In order to obtain the required optical frequency for the ILC, three acousto-optic modulators (AOMs) were employed to shift the frequency of each beam, while also serving a dual role in optical path switching. The cooling LD frequency can be shifted by using a double-pass optical path, corresponding to a detuning from -51.8 MHz to $+18.2$ MHz. The maximum power of the cooling beam reaches up to 424 mW. The repumping LD frequency can be shifted by using a single-pass optical path, corresponding to a detuning from -15.5 MHz to $+19$ MHz. The maximum power of the repumping beam reaches 13 mW. The repumping beam is coupled into the fiber along with the cooling beam and injected into the diffuse cavity via a one-to-four multi-mode fiber with each fiber carrying equal power. The probe beam has the same frequency range as the cooling beam due to their similar layout, and it is injected into the diffuse cavity via a polarization-maintaining (PM) single-mode fiber. The power of the probe beam entering the cavity ranges from 0.4 μW to 24 μW, with a beam diameter of 1 mm, where the power density corresponding to 1 μW is 0.28 mW/cm^2. The power can be adjusted over a wider range by adjusting the setup. The probe beam power from the single-mode fiber is stabilized by using a PID controller with the photodetector (PD1).

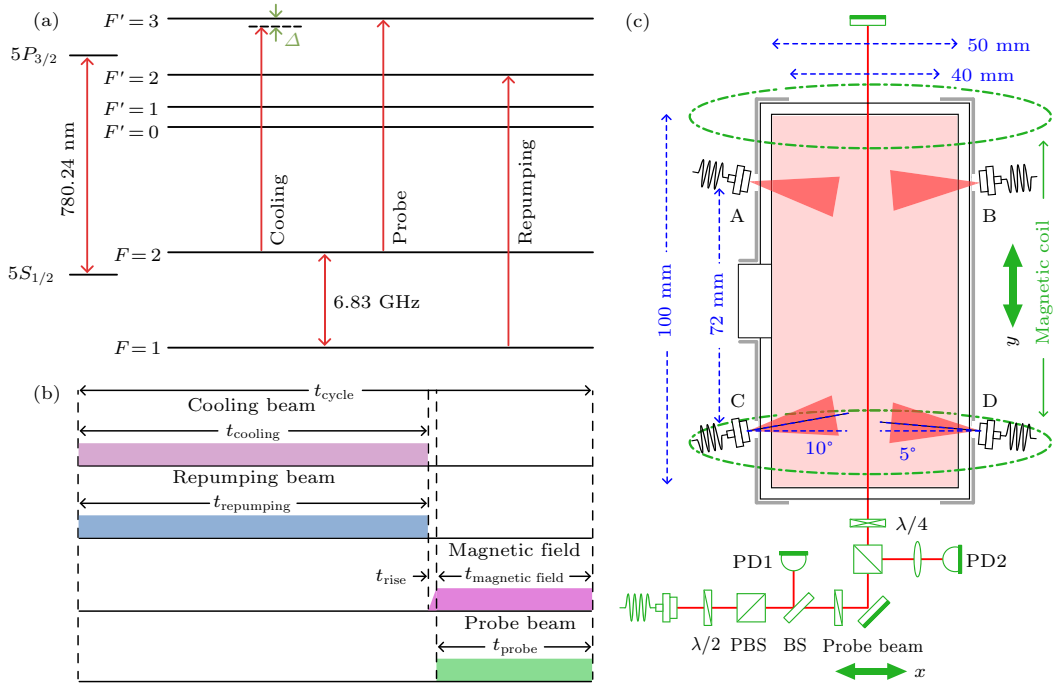


Fig. 1. Schematic diagram of the experimental system: (a) hyperfine energy levels of ^{87}Rb and laser frequency configurations, (b) experimental sequence for atomic distribution detection, and (c) the schematic diagram of the detection system.

The inner dimensions of the diffuse cavity are 100 mm × 50 mm × 6 mm, and the cavity is constructed from 3 mm-thick quartz glass. The cavity is connected to the vacuum system via a hole of 6 mm × 12 mm, maintained at 2×10^{-6} Pa with a 75L ion pump, while the ^{87}Rb atoms are produced using a dispenser activated by direct current (DC). The outer surface of the cavity is covered with a 2-mm-thick diffuse coating, which exhibits a diffuse reflectance of 98% for 780-nm laser. As shown in Fig. 1(c), to inject the cooling and repumping lasers into the cavity, four holes ($\Phi = 2$ mm) are drilled along the long side of the cavity, spaced 72 mm apart. The multi-mode fibers inject the beams at a small angle to promote a uniform optical field distribution. The short side of the cavity features a slit (2 mm × 40 mm) for the probe beam, which can be moved to map the cold atom density throughout the cavity.

The density distribution of cold atoms was measured by using a pair of anti-Helmholtz coils.[21] Each coil has a diameter of 150 mm and consists of 100 turns of 1.5-mm enam-

eled wire. The coils generate a magnetic field gradient of 8.2 Gs/cm (1 Gs = 10^{-4} T) at the center, providing a spatial resolution of about 6 mm for density distribution detection. At this gradient, the magnetic field's switching time is sufficient for the experimental conditions, with a rise time of approximately 450 μs and a much faster fall time achieved via a multilayer magnetic technique.[22] The entire probe optical path and the magnetic coils are mounted on a horizontal mobile platform (HMP) that moves along the x-axis. The magnetic coils are additionally mounted on a vertical mobile platform (VMP) that moves along the y-axis, with the VMP being affixed to the HMP. This configuration allows for 2D mapping of the cold atom density through controlled displacement of the magnetic field and probe arrangement.

A typical time sequence for our experiment is shown in Fig. 1(b). For the cold atom distribution test, once the atoms have been cooled for a duration of $t_{\rm cool}$, the cooling and repumping beams are turned off, and the magnetic field is activated. After a period of $t_{\rm rise}$, the magnetic field has completely stabilized, and the probe beam is turned on to detect the cold atoms. For the optimization of cold atom parameters, the atoms are first cooled by the diffuse laser, after which both beams are turned off, and the probe beam is simultaneously activated to detect absorption.

3. Results and discussion

In our experiment, the circularly polarized probe beam with a power of 2.2 μW and a corresponding power intensity of 0.62 mW/cm^2, traversed through the cavity twice. The density of cold atoms n in the detection area can be calculated by using the equation $\bar{n} = OD/\sigma L$, where L is the length of the area for atom–light interaction. The OD can be calculated using the formula $OD = \ln[(I_{\rm i} - I_{\rm bg})/(I_{\rm o} - I_{\rm bg})]$, where $I_{\rm i}$, $I_{\rm o}$, and $I_{\rm bg}$ represent the incident, transmitted, and background light intensities, respectively. The cross section of the atom–light interaction can be described as[23]

$$\sigma = \frac{\hbar\omega_{\rm L}\Gamma}{2I_{\rm s}} \frac{1}{1 + I/I_{\rm s} + 4(\delta/\Gamma)^2}, \tag{1}$$

where Γ is the natural linewidth, δ is the detuning of the probe beam, $\omega_{\rm L}$ is the frequency of the laser beam, and $I_{\rm s} = 1.669$ mW/cm^2 is the saturation intensity for $|F = 2, m_F = \pm 2\rangle \rightarrow |F = 3, m_F = \pm 3\rangle$ transition, and the calculated cross section is 2.49×10^{-9} cm^2. For this detection system, the density of cold atoms in the detection area is calculated to be 2.01×10^7 cm^{-3} when OD is 1.

The duration of cold atom preparation within the complete experimental cycle can significantly affect performance in quantum sensing and precision measurement, as illustrated by its impact on the Dicke effect in atomic clocks.[24] The ^{87}Rb atoms were effectively cooled from background vapor under diffuse light, and the number of cold atoms saturates with increasing cooling time. The number of cold atoms as a function of cooling time is described by the equation $dN/dt = -\kappa N + \alpha$, where N is the total number of cold atoms in the probe area, κ represents the cold atoms' loss rate, and α describes the rate at which new cold atoms are captured. With the power and frequency of both the cooling beam and the repumping beam held constant, the number of detected cold atoms increases with increasing cooling time, as shown in Fig. 2(a). We measured the absorption of cold atoms as the cooling times increased for different cooling powers. By fitting the data to the equation $N(t) = \alpha/\kappa(1 - e^{-\kappa(t-t_0)})$, where $N(\infty) = \alpha/\kappa$ represents the saturated number of cold atoms, we deduced that the loss rates were 15.7 s^{-1}, 15.1 s^{-1}, 13.7 s^{-1}, 13.1 s^{-1}, 12.0 s^{-1}, 11.9 s^{-1}, 9.2 s^{-1}, corresponding to cooling power ranging from 280 mW to 40 mW, respectively, the loss rate was positively correlated with the density of cold atoms. We fitted the loss rate and loading rate, which exhibit a linear relationship as shown in Fig. 2(b). With the ILC method, the density of alkali metal vapor is relatively high, while the vacuum level of our system is not optimal due to technical constraints. Consequently, collisions between cold atoms and background gas constitute the dominant loss channel.

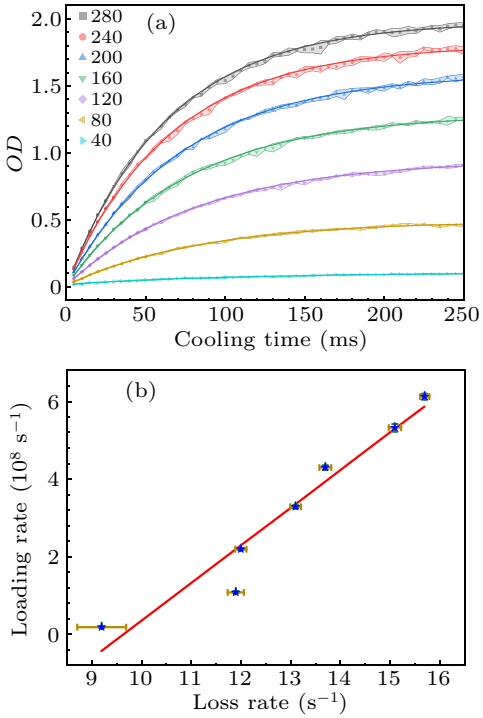


Fig. 2. (a) Experimental data of optical depth along the optical detection axis *versus* cooling time. (b) The relationship between loading rate and loss rate at different cooling powers.

After the cooling beam has been switched off, cold atoms decay due to collisions with background atoms and other cold atoms.[25,26] We set the cooling time to 300 ms, at which point saturation is achieved, and the cooling and repumping powers are set to 280 mW and 13 mW, respectively. The frequency of

the cooling beam is red-detuned by 15 MHz for the transition from $|F=2\rangle$ to $|F'=3\rangle$, which is the optimized frequency for achieving a maximum number of cold atoms. The frequency of the repumping beam corresponds to the resonance of the $|F=1\rangle$ to $|F'=2\rangle$ transition. As shown in Fig. 3, the probe beam is turned on $t_{\rm p}$ seconds after the cooling beam has been switched off to measure the absorption of cold atoms. Each data set is obtained under the same cooling power and detuning conditions. The cold atoms decay within approximately 30 ms, exhibiting an exponential decay. The remaining cold atoms in the probe beam area can be described as[27]

$$s(r,t_{\rm p}) = \mathcal{C} \times \left[1 - \exp\left(-\frac{m(r/t_{\rm p})^2}{2k_{\rm B}T}\right)\right], \tag{2}$$

where $\mathcal{C}$ is a normalization constant, r is the radius of the probe beam, $k_{\rm B}$ is the Boltzmann constant, and T is the temperature of the cold atomic cloud. The temperature of the cloud can be fitted as 10 μK using Eq. (2), which is below the Doppler limit temperature due to a sub-Doppler cooling mechanism.

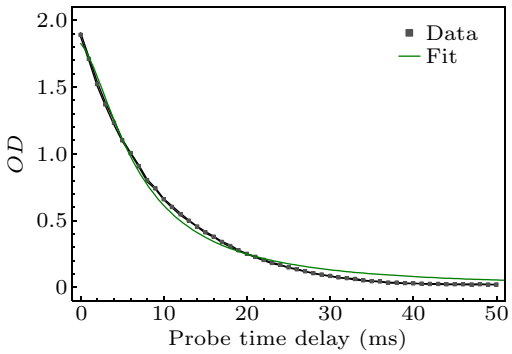


Fig. 3. Measured optical depth at different probe time delays.

Unlike other cavity geometries, the absorption of cold atoms in the flat cavity does not exhibit the characteristic known as TOF (time of flight).[28] This phenomenon occurs when cold atoms, initially located above the probe beam, fall into the probe beam area due to gravitational effects, resulting in secondary absorption. However, in the flat cavity, only a few cold atoms are present in the upper region, resulting in negligible secondary absorption.

The volume of the diffuse cavity significantly affects the power density within it, which is inversely proportional to the cavity's size.[29] The light distribution is influenced by the geometry of the cavity, the mode of fiber injection, and the size and number of apertures used for the fiber and vacuum connections. For different cavity geometries used in ILC, the saturated power and optimal laser frequency required to achieve a maximum number of cold atoms often vary. Therefore, it is essential to measure the saturation power and optimal laser frequency for each unique cavity configuration.

We keep the repumping and probe beams at their resonant frequencies, with powers of 13 mW and 2.2 μW, respectively. We first investigate the effect of cooling frequency on absorption while keeping the cooling power at 270 mW. As shown in Fig. 4(a), ILC demonstrates a large velocity capture capability; atoms with velocity v can be cooled using a laser with a detuning frequency $|\Delta| \leq kv \leq 2|\Delta|$, where k is the wave vector. The cooling beam with a detuning of −15 MHz exhibits the best cooling efficiency, and lasers with ±10-MHz detuning can also cool atoms effectively. The power of the cooling laser is another principal factor affecting the number of cold atoms. As the power of the cooling laser increases, with the red detuning fixed at −15 MHz, the number of cold atoms rises until the cooling power reaches saturation. When the power exceeds 300 mW, no further significant increase in absorption is observed, as shown in Fig. 4(d).

For the repumping laser used to clear dark states and enable recycling transitions, the requirement for the repumping power is not as high compared to the cooling laser. However, the power does influence the number of atoms significantly. In this study, the power and the detuning of the cooling laser are kept at 270 mW and −15 MHz, respectively, while the power intensity of the probe beam is 0.62 mW/cm^2. As shown in Fig. 4(b), the number of cold atoms exhibits insignificant changes within the range of ±15 MHz. The number of cold atoms increases significantly with several mW and stabilizes when the power of the repumping laser reaches about 4 mW, as shown in Fig. 4(e).

The intensity of the probe beam is comparatively low, requiring only several μWs, and is set to the resonant frequency of the transition. However, when we change the detuning of the probe beam, the atomic absorption follows a Lorentzian profile, and the Lorentzian fit results in a full width at half maximum (FWHM) of 10.3 MHz, as shown in Fig. 4(c). On the other hand, we vary the power intensity of the probe beam, as shown in Fig. 4(f), we observe that as the power intensity of the probe beam increases, the number of cold atoms decreases. Therefore, during the detection process, the probe beam should have appropriately low power density to avoid inaccuracies in signal measurement caused by excessively high probe light power intensity.[30]

Although cold atoms are not trapped by the light field in ILC, previous experiments have demonstrated that the distribution of cold atoms is closely linked to the intensity profile of the light field. Furthermore, the overall motion of the atoms is constrained by the shape of the cavity. We utilized a detection system with the capability for 2D movement (along the x and y axes) to measure the distribution of cold atoms, achieving a spatial resolution of approximately 6 mm. By moving the magnetic field and the detection light path, we measured the distribution of cold atoms within the ±16 mm × ±45 mm area inside the cavity, with several extraction lines drawn, each corresponding to the atomic density distribution at various positions, as shown in Fig. 5.

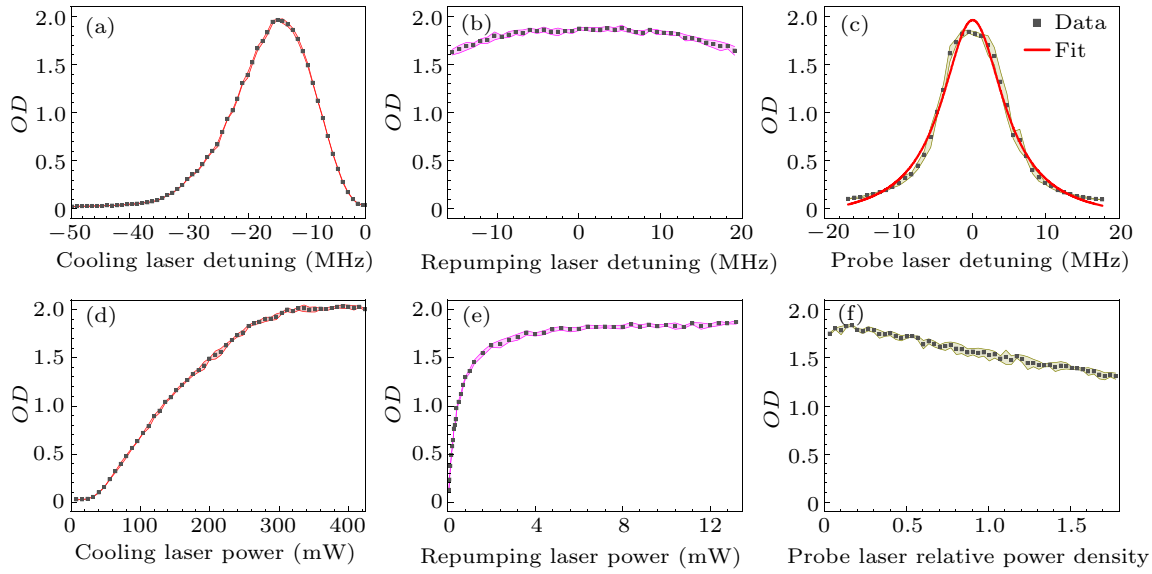


Fig. 4. Experimental data of *OD* along the optical detection axis *versus* cooling parameters. (a) The dependence of cooling light detuning on *OD* at 270 mW cooling power. (b) The dependence of repumping light detuning on *OD* at 13-mW repumping power. (c) The dependence of probe light detuning on *OD* at 0.62-mW/cm^2 probe power intensity. (d) *OD versus* cooling light power with the cooling laser at −15-MHz red detuning. (e) *OD versus* repumping light power with the repumping laser at resonance. (f) *OD versus* probe light power with the probe laser at resonance.

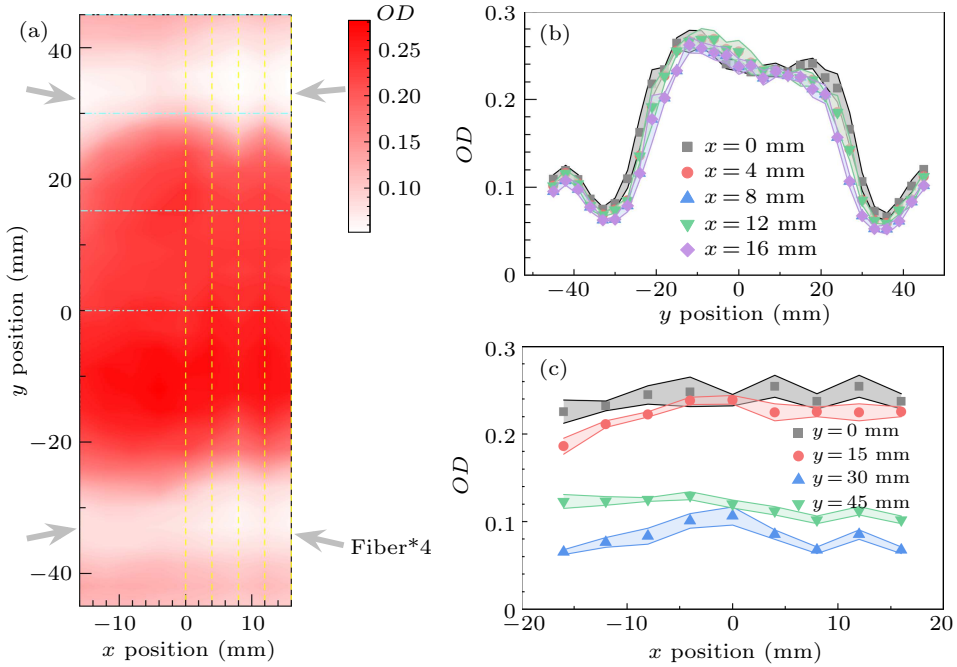


Fig. 5. Measurement of spatial distribution of cold atoms. (a) Atomic density distribution at different positions within the ±16 mm × ±45 mm region of the cavity. (b) Atomic density along the *y*-direction at different *x* positions (yellow dashed line). (c) Atomic density along the *x*-direction at different *y* positions (cyan dashed line).

Since the cold atoms are constrained by the cavity's size, they form a sheet-like cloud with a relatively uniform distribution at the center, exhibiting a q2D distribution in certain areas. The cold atomic distribution along the x direction at the same y position demonstrates relative uniformity, with minor fluctuations across different locations. However, the distribution along the y direction at the same x position exhibits more pronounced variations, particularly in the region $y = \pm 33$ mm, where the weakest absorption is observed despite the cooling light intensity being relatively stronger compared to other positions, corresponding to the locations of the fiber injection. This phenomenon has been observed in previous experiments, explained by the cooling beam pushes atoms away from the injection area. Furthermore, we also mitigated the potential for such issues arising from light leakage by employing mechanical switches. Additionally, to improve the vacuum level, vacuum glue was applied at the connecting seams before the application of the diffuse coating, which may lead to field asymmetry; further optimization can be achieved by adjusting the light injection mode.

4. Conclusion

In this study, we have designed and implemented a flat chamber for ILC aimed at quantum sensing applications. We systematically characterized the key parameters and examined the effects of fundamental factors within this newly shaped cavity. Using a detection system based on a movable gradient magnetic field, we mapped a 2D distribution of cold atoms, which revealed a uniform distribution in the center of the cavity. Our experiments provided a detailed understanding of the fundamental physical processes of ILC in this system. We hope that our efforts will advance the application of ILC in quantum sensing and quantum precision measurement.

Acknowledgements

Project supported by the National Natural Science Foundation of China (Grant No. 92165107), the China Postdoctoral Science Foundation (Grant No. 2022M723270), and the National Defense Basic Scientific Research Pogram of China.

References

[1] Hagley E W, Deng L, Kozuma M, Trippenbach M, Band Y B, Edwards M, Doery M, Julienne P S, Helmerson K, Rolston S L and Phillips W D 1999 *Phys. Rev. Lett.* **83** 3112
[2] O'Hara K M, Hemmer S L, Gehm M E, Granade S R and Thomas J E 2002 *Science* **298** 2179
[3] Liu L, Lü D S, Chen W B, Li T, Qu Q Z, Wang B, Li L, Ren W, Dong Z R, Zhao J B, Xia W B, Zhao X, Ji J W, Ye M F, Sun Y G, Yao Y Y, Song D, Liang Z G, Hu S J, Yu D H, Hou X, Shi W, Zang H G, Xiang J F,Peng X K and Wang Y Z 2018 *Nat. Commun.* **9** 2760
[4] Lü D S, Ren W, Sun Y, Li T, Qu Q Z, Wang B, Li L, Zhao J B, Zhao X, Ji J W, Ye M F, Xiang J F, Chen W B, Wang Y Z and Liu L 2022 *Natl. Sci. Rev.* **10** nwac180
[5] Deng S M D, Ren W, Xiang J F, Zhao J B, Li L, Zhang D, Wan J Y, Meng Y L, Jiang X J, Li T, Liu L and Lü D S 2024 *Chin. Phys. B* **33** 070602
[6] Guillot E, Pottie P E and Dimarcq N 2001 *Opt. Lett.* **26** 1639
[7] Wang X C, Cheng H D, Xiao L, Zheng B C, Meng Y L, Liu L and Wang Y Z 2012 *Chin. Opt. Lett.* **10** 080201
[8] Langlois M, Sarlo L D, Holleville D, Dimarcq N, Schaff J F and Bernon S 2018 *Phys. Rev. Appl.* **10** 064007
[9] Yin Y R, Xu A N, Peng J and Liu B 2025 *Chin. Phys. B* **34** 023401
[10] Ouyang X C, Yang B W, Hu Q Q, Qi H H, Xiao L, Wan J Y and Cheng H D 2021 *Phys. Rev. A* **103** 043118
[11] Meng Y L, Jiang X J, Wu J, Ye M F, Cheng H D, Li L and Liu L 2022 *Front. Phys.* **10**
[12] Wang X, Sun Y and Liu L 2021 *Opt. Express* **29** 43435
[13] Wang W L, Deng J Lan and Wang Y Z 2015 *J. Opt. Soc. Am. B* **32** 2441
[14] Wang X, Sun Y and Liu L 2022 *Photon. Res.* **10** 1947
[15] Esnault F X, Holleville D, Rossetto N, Guerandel S and Dimarcq N 2010 *Phys. Rev. A* **82** 033436
[16] Liu P, Meng Y L, Wan J Y, Wang X M, Wang Y N, Xiao L, Cheng H D and Liu L 2015 *Phys. Rev. A* **92** 062101
[17] Wan J Y, Wang X, Zhang X, Meng Y L, Wang W L, Sun Y and Liu L 2022 *Phys. Rev. A* **105** 033110
[18] Meng Y L, Cheng H D, Zheng B C, Wang X C, Xiao L and Liu L 2013 *Chin. Phys. Lett.* **30** 063701
[19] Meng Y L, Cheng H D, Liu P, Zheng B C, Xiao L, Wan J Y, Wang X M and Liu L 2014 *Phys. Lett. A* **378** 2034
[20] Sun Y 2024 *Sci. China-Phys. Mech. Astron.* **67** 120311
[21] Wang X C, Cheng H D, Xiao L, Zheng B C, Meng Y L, Liu L and Wang Y Z 2018 *Chin. Phys. Lett.* **29** 023701
[22] Zhang X, Qin Q, Fan X Y, Yang B W, Wang X, Wang W L, Sun Y and Liu L 2024 *Rev. Sci. Instrum.* **95** 064703
[23] Steane A M, Chowdhury M and Foot C J 1992 *J. Opt. Soc. Am. B* **9** 2142
[24] Sun X L, Zhang J W, Cheng P F, Zuo Y N and Wang L J 2018 *Chin. Phys. B* **27** 023101
[25] Zhang W Z, Wang X C, Cheng H D, Xiao L, Liu L and Wang Y Z 2009 *Chin. Phys. Lett.* **26** 083703
[26] Huang J Q, Zhang J W, Wang S G, Wang Z B and Wang L J 2015 *Chin. Phys. B* **24** 113701
[27] Wang X, Sun Y, Cheng H D, Wan J Y, Meng Y L, Xiao L and Liu L 2020 *Phys. Rev. Appl.* **14** 024030
[28] Cheng H D, Zhang W Z, Ma H Y, Liu L and Wang Y Z 2009 *Phys. Rev. A* **79** 023407
[29] Crowther B G 1996 *Appl. Opt.* **35** 5880
[30] Zheng B C, Cheng H D, Meng Y L, Liu P, Wang X M, Xiao L, Wan J Y and Liu L 2014 *Mod. Phys. Lett. B* **28** 1450116